



Physically defined long-term and short-term synapses for the development of reconfigurable analog-type operators capable of performing health care tasks

Yongsuk Choi¹, Dong Hae Ho², Seongchan Kim^{3,4}, Young Jin Choi⁵, Dong Gue Roe⁶, In Cheol Kwak⁵, Jihong Min¹, Hong Han¹, Wei Gao^{1*}, Jeong Ho Cho^{5*}

Extracting valuable information from the overflowing data is a critical yet challenging task. Dealing with high volumes of biometric data, which are often unstructured, nonstatic, and ambiguous, requires extensive computer resources and data specialists. Emerging neuromorphic computing technologies that mimic the data processing properties of biological neural networks offer a promising solution for handling overflowing data. Here, the development of an electrolyte-gated organic transistor featuring a selective transition from short-term to long-term plasticity of the biological synapse is presented. The memory behaviors of the synaptic device were precisely modulated by restricting ion penetration through an organic channel via photochemical reactions of the cross-linking molecules. Furthermore, the applicability of the memory-controlled synaptic device was verified by constructing a reconfigurable synaptic logic gate for implementing a medical algorithm without further weight-update process. Last, the presented neuromorphic device demonstrated feasibility to handle biometric information with various update periods and perform health care tasks.

Copyright © 2023 The Authors, some rights reserved; exclusive licensee American Association for the Advancement of Science. No claim to original U.S. Government Works. Distributed under a Creative Commons Attribution NonCommercial License 4.0 (CC BY-NC).

INTRODUCTION

In the era of big data, high volumes of biometric data are generated and updated in real time by wearable devices (1–8). Processing the aggregated data for personalized and precision health care is a major challenge, requiring highly specialized human and computing resources (9–11). While extensive efforts have been made toward developing bioelectronic devices such as wearable sensors (12–16), implantable devices (17, 18), and wireless communication systems (19, 20) for precisely acquiring large amounts of biosensor data, there is a lack of sophisticated computing systems for processing the data. Conventional computing systems based on von Neuman architecture are impractical for processing large amounts of unstructured data as the processor needs to communicate with the memory to perform each operation, leading to wasted energy and time resources (21–23). On the other hand, emerging neuromorphic computing systems that can perform parallel operations with merged memory and processing units, such as the brain, serve as an attractive solution (24–28).

Neuromorphic devices that electronically simulate the functions of biological synapses in human neural networks have been reported (29–39). These artificial synapses, characterized by their low power consumption, small volume, and optimized analog signal processing capabilities, have excellent potential to process overflowing biometric data. Artificial synapses exhibit short-term plasticity

(STP) and long-term plasticity (LTP), enabling the processing and memorization of data throughout multiple periods and cycles. STP is a temporal change in synaptic weight generated by updating signals, enabling efficient computing functions in artificial neural networks (ANNs) (Fig. 1A). On the other hand, LTP is a retentive change in synaptic weights, which lasts longer and is responsible for memory and learning abilities in ANNs (Fig. 1B). Various neuromorphic computing, artificial intelligence, and soft robotics studies have been reported on the basis of artificial synapses that display STP and LTP (30, 32, 34, 37, 40, 41). Most reported artificial synapses exhibit STP on small input signals and LTP on higher energy or repeated input signals. Therefore, to take advantage of both STP and LTP in synaptic devices of an ANN and to provide high-order functionalities such as artificial intelligence, ANNs must be repetitively trained with numerous datasets (30, 37, 40, 42, 43). As a result, research on ANNs is highly dependent on software algorithms and large volumes of qualified database resulting vast and complex computing resources. Developing simplified and functionally flexible neuromorphic processors that meet the increasing demand for neuromorphic computing can be a differentiated solution.

Here, we present the implementation of a simplified, functionally flexible analog-type operator by physically defining STP and LTP in a crossbar synapse array. The synapses underlying the processor are electrolyte-gated vertical organic transistors that contain a photoreactive cross-linker to control the ionic permeability of the channel. All synapses in the synaptic processor are fabricated simultaneously and then selectively exposed to ultraviolet (UV) light to form short-term synapse (STS) and long-term synapse (LTS) (Fig. 1C). In addition, the degree of photochemical cross-linking is adjusted by changing the UV exposure time to precisely control the memory properties of the synapses. Last, the applicability of the neuromorphic processor consisting of STS and LTS is evaluated by constructing a small-sized analog-type operator to conduct

¹Andrew and Peggy Cherng Department of Medical Engineering, California Institute of Technology, Pasadena, CA 91125, USA. ²Mechanical Engineering, Soft Materials and Structures Lab, Virginia Tech, Blacksburg, VA 24061, USA. ³SKKU Advanced Institute of Nanotechnology (SAINT), Sungkyunkwan University, Suwon 16419, Korea. ⁴Department of Engineering Science and Mechanics, The Pennsylvania State University, University Park, PA 16802, USA. ⁵Department of Chemical and Biomolecular Engineering, Yonsei University, Seoul 03722, Republic of Korea. ⁶School of Electrical and Electronic Engineering, Yonsei University, Seoul 03722, Republic of Korea.

*Corresponding author. Email: weigao@caltech.edu (W.G.); jhcho94@yonsei.ac.kr (J.H.C.)

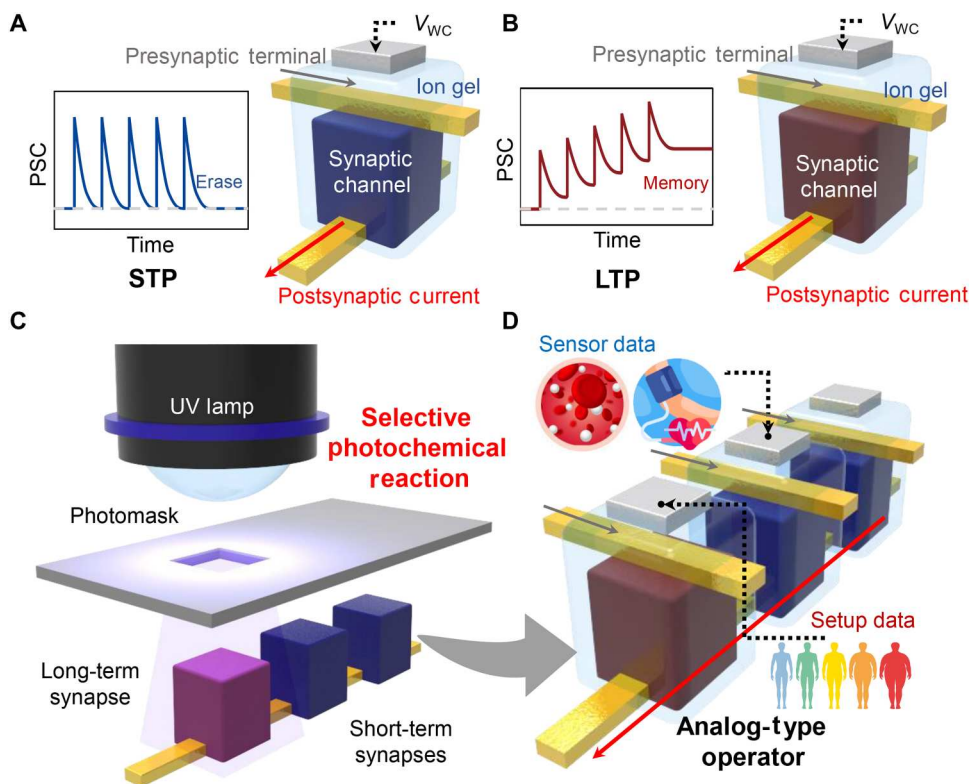


Fig. 1. Flexible analog-type operator enabled by selective definition of short-term synapse (STS) and long-term synapse (LTS). (A and B) Schematic illustration of synaptic devices showing (A) STP and (B) LTP. (C) Selectively cross-linked organic synaptic channel via a photochemical reaction. (D) Schematic demonstration of a small-sized analog-type operator consisting of an LTS and STS. PSC, postsynaptic current.

representative data-processing tasks for wearable health care devices (Fig. 1D): (i) The processor based on synaptic devices implements the biomedical algorithm for diagnosing metabolic syndrome in hardware by performing the reconfigurable Boolean logic function through the long-term synaptic switch. (ii) Static and nonstatic bio-signals are processed on the basis of the memory and processing functions of the LTS and STS to support human metabolism as a wearable neuromorphic computer.

RESULTS

Demonstration of the synaptic devices

As an essential component of an ANN, the artificial synaptic device with a vertical crossbar structure that is highly beneficial for three-dimensional (3D) integration is shown in Fig. 2A. The vertical synapse consists of an organic semiconductor [poly(3-hexylthiophene) (P3HT)] that is located at the intersection of the top electrodes, bottom electrodes, and electrolytes surrounding the channel. A voltage pulse applied through the gate electrode in contact with the electrolyte evokes the penetration of ions into the organic synaptic channel, resulting in synaptic current behaviors in the crossbar synaptic device. The detailed mechanism of ion permeability into vertical organic channels was discussed in previous reports (42, 44, 45). Furthermore, the movement of ions penetrating the organic channel is highly controllable by selectively binding the cross-linking agent to the alkyl chain of P3HT (Fig. 2B). Figure 2C shows the excitatory postsynaptic current (EPSC) behaviors of

synaptic devices with different retention times. Typically, STP of synaptic devices is defined as synaptic plasticity that disappears within several seconds, while LTP refers to changes that persist for tens of seconds or longer. Here, we define synaptic device that exhibits STP under the fixed pulse stimulation as STSs and components that exhibit LTP as LTSs. The channels of the STSs and LTSs were both composed of P3HT and ethane-1,2-diyl bis(4-azido-2,3,5,6-tetrafluorobenzoate) (2Bx) cross-linker. The LTS was defined by inducing cross-linking reactions of 2Bx under UV light. The amplitude of the applied voltage pulses varied from -0.5 to -3 V and the width of the pulses was fixed at 30 ms. The read voltage applied to the postsynaptic terminal was set to -0.01 V. The postsynaptic current (PSC) of the STS decayed rapidly to its original level due to the high degree of freedom of ion movement through the abundant free volume of P3HT (Fig. 2C, top). On the other hand, the PSC of the LTS decayed slowly for over 10 s as the cross-linking agent bound to the free volume of P3HT restricted the movement of ions (Fig. 2C, bottom). The difference in retention characteristics becomes more evident as the number of applied pulses increases. Figure 2D plots the PSC of the STS (black line) and LTS (red line) under 10 consecutive pulse sets of -3 V. After the application of the pulses, the PSC of the STS peaked at $50\ \mu\text{A}$ and immediately returned to its baseline level within 60 s. On the other hand, the LTS exhibited a relatively lower peak current of $37\ \mu\text{A}$ and a clear retention current of $5.3\ \mu\text{A}$ after the same time. On the basis of this, we classify synaptic devices into STS and LTS, using 60 s as the criterion for the duration of synaptic plasticity. Next, the cross-

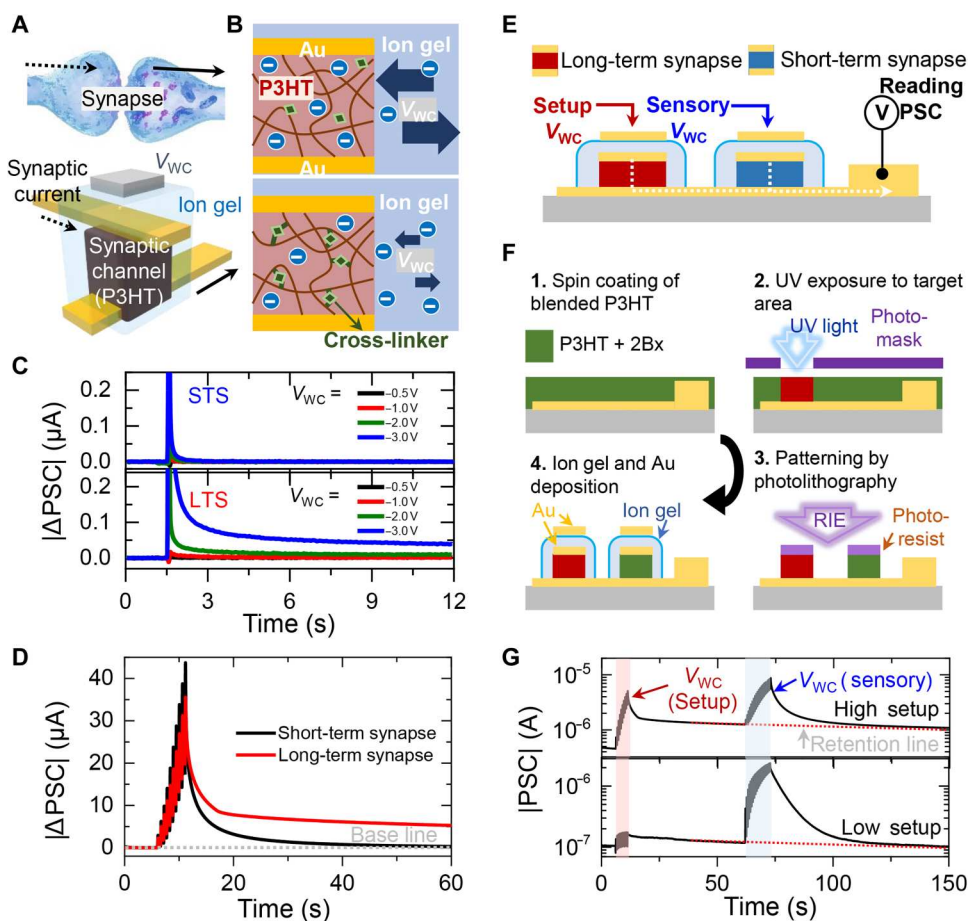


Fig. 2. The design and characterization of the ion gel-gated vertical crossbar synapse array. (A) Schematic diagram of ion gel-gated vertical crossbar transistor array mimicking biological synapse. (B) Cross-sectional schematic of ion movement between organic channels and ion gel with and without a cross-linking agent. (C) Excitatory postsynaptic current (EPSC) responses of the short-term synapse (STS) (top) and long-term synapse (LTS) induced by the application of varied V_{WC} . (D) A real-time plot of postsynaptic currents (PSCs) of STS (black line) and LTS (red line) under 20 consecutive potentiation pulses ($V_{WC} = -3$ V). (E) Cross-sectional schematic image of a small-sized neural network consisting of LTS and STS. (F) The fabrication procedure of the crossbar array through a selective photochemical reaction. (G) The output PSC response of the small-sized neural network device under the sequent update of LTS and STS.

sectional diagram of a crossbar synapse array consisting of an LTS and an STS for simulating the integrated data processing property of a biological neural network is presented in Fig. 2E. The fabrication procedure of the crossbar array is described in Fig. 2F. A P3HT solution containing 5 weight % of 2Bx dissolved in chloroform at a concentration of 5 mg/ml was spin-coated on the as-prepared substrate that has 3/17-nm-thick Cr/Au bottom electrode lines. After selectively exposing the LTS channel to UV light, the synaptic channels were defined by a conventional photolithography process. Next, the top electrodes, ion gel, and gate electrodes were deposited to form the electrolyte-gated synaptic transistor. Figure 2G plots the output current behavior of the small-sized 2 × 1 synapse array as a function of time. The base current of the synapse array was updated by 10 consecutive pulses applied through the gate terminal of the LTS. The lower base current was set by applying low-amplitude pulses set of −1 V, while the higher base current was generated by applying high-amplitude pulses of −3 V, as shown in the bottom and top panels of Fig. 2G, respectively. After the stabilization of the synaptic current, 10 consecutive pulses of −3 V were applied to the STS. In both cases, the output PSC of the synapse array

showed the transient spikes that lasted less than 1 min originated from STS accumulated on the retention current lasting more than several minutes. Overall, the retention characteristics of the synaptic devices were successfully modulated by a simple UV exposure process despite consisting of the same material and structure. This represents a successful demonstration of photochemically controlled ion penetration through a cross-linker in crossbar synaptic devices and its consequent impact on synaptic characteristics. Furthermore, the multiperiodic data processing capability of biological neural networks was successfully implemented in an artificial synapse array.

Optimization of retention properties

To achieve optimized long-term properties of LTSSs for further data processing applications, we precisely investigated varying degrees of photoreactive cross-linking and corresponding synaptic properties. Figure 3A showed the schematic illustration of the detailed P3HT channel cross-linked by 2Bx and the underlying steps of the chemical reaction (42, 46–48). The azide group of 2Bx is photolyzed to produce inert nitrogen gas and highly reactive singlet nitrene (−1

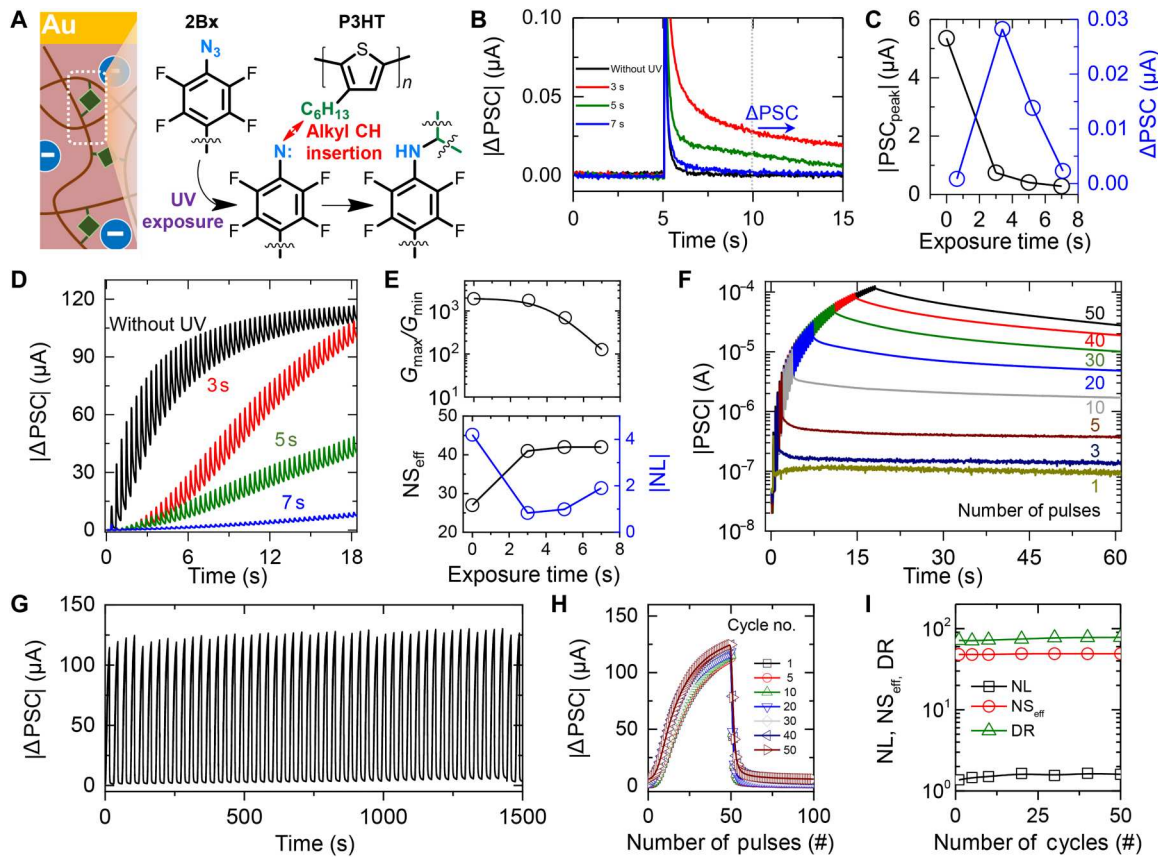


Fig. 3. Optimization of long-term plasticity (LTP) of the vertical synapse through photochemical reaction control. (A) Schematic illustration of the photochemical cross-linking reaction between ethane-1,2-diyi bis(4-azido-2,3,5,6-tetrafluorobenzoate) (2Bx) and poly(3-hexylthiophene) (P3HT). (B) Excitatory postsynaptic current (EPSC) responses of organic synapse under varied photochemical reaction time. (C) A plot of extracted peak postsynaptic current (PSC) and retention PSC values as a function of the ultraviolet (UV) exposure time. (D) Long-term potentiation characteristics of cross-linking-controlled synaptic devices under the application of 50 potentiation pulses. (V_{WC} pulses with amplitudes of -3 V). (E) Plots of the dynamic range ($G_{\text{max}}/G_{\text{min}}$), $|\text{nonlinearity} (\text{NL})|$, and effective number of states (NS_{eff}) as functions of the reaction time. (F) Long-term potentiation and retention plot under the varied number of potentiation V_{WC} values of LTS with 3-s photochemical reaction time. (G) Long-term potentiation and depression (LTP/D) characteristics of the LTS over 50 cycles. Each cycle consists of 50 potentiation pulses ($V_{\text{WC}} = -3$ V), followed by 50 depression pulses ($V_{\text{WC}} = 2$ V). (H) Cycle-to-cycle variations of LTP/D curve for 50 cycles. (I) Plots of extracted dynamic range (DR), NL, and NS_{eff} during the 50 LTP/D cycles.

Downloaded from https://www.science.org on July 06, 2023

N) under UV irradiation. The generated singlet nitrene is inserted by preferentially reacting with the C—H bond in the alkyl chain present in the P3HT. The photochemical reaction between 2Bx and P3HT was confirmed by Fourier transform infrared spectroscopy under varying UV irradiation times (fig. S1). The specific vibrational peak of the azide group located at 2125 cm^{-1} gradually decreases as the irradiation time increases from 0 to 7 s, indicating the photolyzing of the azide group. Figure 3B shows the EPSC responses of cross-linked P3HT vertical synapses exposed under varying UV exposure times of 0, 3, 5, and 7 s. Vertical synapses with varying UV exposure times of 0, 3, 5, and 7 s were prepared simultaneously on a single substrate. The voltage pulse having an amplitude of -3 V and 30-ms width was applied through the gate terminal after 5 s from the beginning of the measurement. The read voltage was set to -0.01 V. While all vertical synapses displayed EPSC that spiked and gradually decreased after excitation as a function of time, there were noticeable differences in peak height and retention current. Figure 3C plots the peak current (black) and retention current (blue) as a function of the UV irradiation time. The retention current was recorded 5 s after the application of the pulsed

voltage. The synapse without UV irradiation showed the largest peak current of $5.3\text{ }\mu\text{A}$, and the peak current decreased rapidly as the irradiation time increased. On the other hand, the retention current of the synapse without UV irradiation was the smallest, while the largest retention current was shown in the synapse exposed to UV for 3 s. These trends in peak current and retention behavior correspond to the difference between on current and hysteresis window of the transfer curves of synaptic transistors as shown in fig. S2. As the photocrosslinking reaction progressed with increasing the UV exposure time, the on-current of the synaptic transistor decreased, while the hysteresis window increased. Here, the on-current of the transfer curves and peak current of EPSC responses refer to the amount of ion penetration into the P3HT channel. The increasing hysteresis window indicates inhibited ion mobility. The overall results indicate that 2Bx cross-linked to P3HT by photochemical reactions controls the movement of ions through the synaptic channel. The 2Bx molecules bind to the free volume of the P3HT polymer chain and suppress the ion flow between the P3HT and ion gel resulting decrease in peak PSC while increasing the retention current.

The effect of photochemical cross-linking on long-term potentiation characteristics of the synapse was further analyzed. Figure 3D shows the real-time PSC plots of synapses with varied photochemical reaction times under 50 consecutive pulses. The synapse without cross-linking displayed a log-linear PSC response where the current increased after the initial pulse update and slowly converted to a maximum conductance state. On the other hand, photochemically cross-linked synapses showed a constant linearly increasing curve after being suppressed during the initial pulses. As key parameters for evaluating the data processing capability of a synapse, dynamic range (G_{\max}/G_{\min}), nonlinearity (NL), and the effective number of states (NS_{eff}) were additionally analyzed from the long-term potentiation curves as shown in Fig. 3E. The detailed method for calculating the G_{\max}/G_{\min} , NL, and NS_{eff} are described in figs. S3 and S4 and Materials and Methods. As the degree of photochemical reaction increased, the G_{\max}/G_{\min} of the long-term potentiation curve decreased, and thus, the device without cross-linking exhibited the largest G_{\max}/G_{\min} of 1.9×10^3 . However, in terms of linear update characteristics, the performance of photo-crosslinked synapses was superior as shown in NL and NS_{eff} . In

particular, the synapse photocrosslinked for 3 s exhibited the most excellent long-term potentiation characteristics, attaining a desirable NL of 0.83 and an NS_{eff} of 42 while maintaining a high dynamic range over 1000. To confirm the stability of the photocross-linked synapse, we evaluated the retention properties for each memory state (Fig. 3F). Beginning from the same base current, each memory state was accessed by applying a varying number of pulses ranging from 1 to 50. In the update region where the pulses were applied through the gate terminal, deviations in current were negligible. Furthermore, each current state formed by varying the number of pulses remained parallel without overlapping, showing a distinguishable difference between the states.

To further verify the reliability of the photocrosslinked synapse, we repeatedly measured long-term potentiation and depression (LTP/D) characteristics under 50 potentiation cycles, followed by 50 depression cycles. The potentiation and depression voltage for the LTP/D curve was set to -3 and 2 V, respectively. The depression voltage of 2 V was selected to have better reproducibility during the repeated cycle test (fig. S5). The real-time PSC responses during 50 LTP/D cycles (a total of 5000 update pulses) are shown in Fig. 3G.

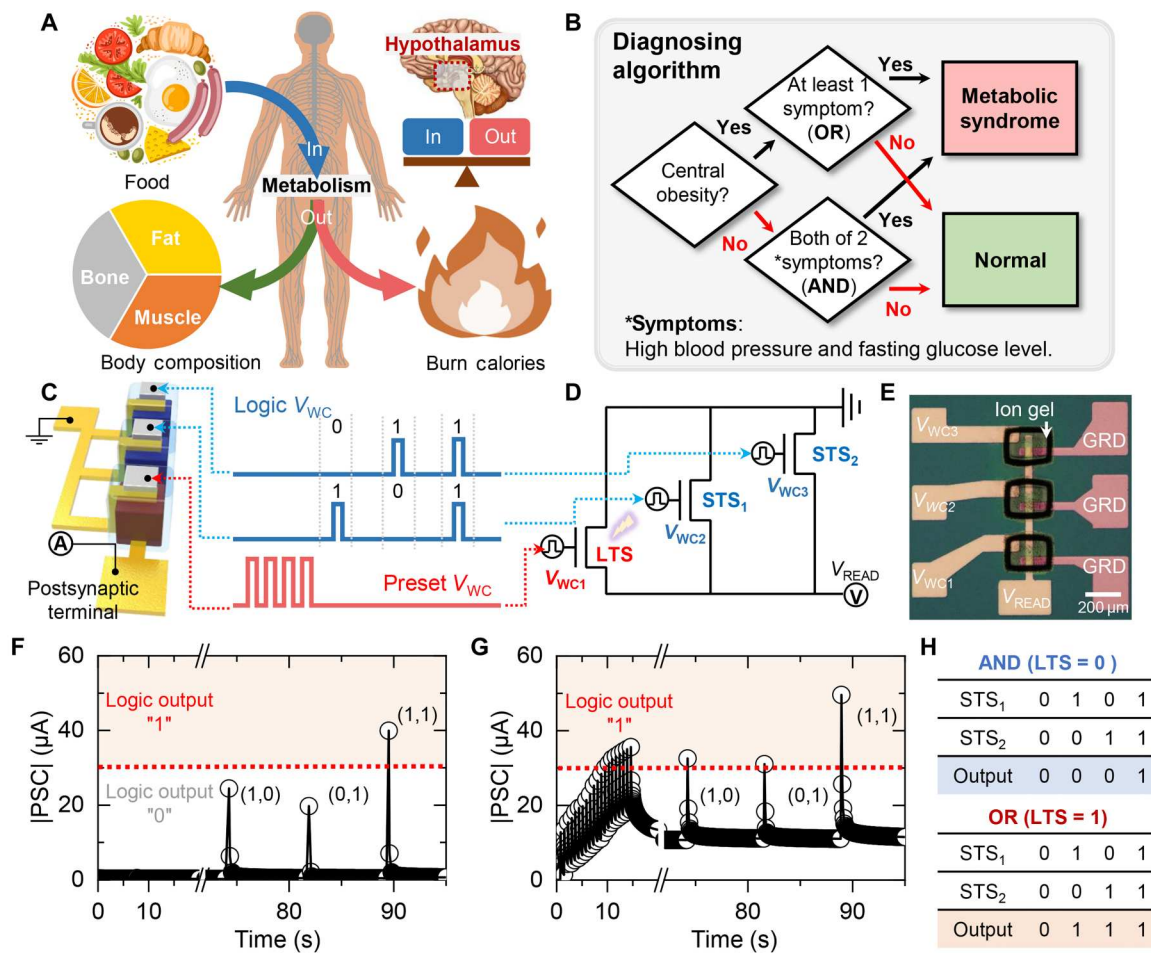


Fig. 4. Reconfigurable Boolean logic implementing diagnosing algorithm for metabolic syndrome. (A) Schematic illustration of human metabolism. (B) Simplified medical algorithm for diagnosing metabolic syndrome. (C) Proof-of-concept illustration of reconfigurable synaptic logic gate consists of long-term synapse (LTS) and short-term synapses (STSs). (D and E) Circuit diagram (D) and optical microscope image (E) of the reconfigurable synaptic logic. The GRD indicates the ground, i.e. source. (F) Real-time |postsynaptic current (PSC)| response of the reconfigurable synaptic logic under varied logic input at AND mode. (G) Output |PSC| response of the reconfigurable synaptic logic switched to OR mode via training the LTS. (H) The truth table of AND/OR logic gates for the reconfigurable synaptic logic gate.

Our optimized long-term vertical synapse showed reliable LTP/D characteristics without any sign of breakdown or errors. Figure 3H shows the LTP/D plot of extracted PSC states as a function of the pulse number. The detailed method for extracting each state from a real-time LTP/D curve is described in fig. S6. Representative LTP/D curves from the 50 cycles were overlapped to confirm that the device has negligible cycle-to-cycle variation. In addition, key parameters including G_{\max}/G_{\min} , NL, and NS_{eff} calculated from the LTP/D curves remained constant during the repeatability test (Fig. 3I). The reliability of the device during the potentiation and depression process was further investigated under the application of irregular pulse sets as shown in fig. S7. Overall, the presented vertical organic synapse with optimized photochemical cross-linking for 3-s UV exposure showed highly stable weight update and retention behaviors, comparable to that of other synaptic devices used for neuromorphic computing tasks.

Biomedical application of the analog-type operator

Next, the development of an analog-type operator composed of STS and optionally transformed LTS to be used as a computing tool for biomedical applications is presented. To fully use the described features of LTS and STS, we selected a biological task requiring integrated processing of static and nonstatic biomarker data from multiple sources: metabolic homeostasis sustained by the human brain. Metabolism is the conversion of ingested food into chemical energy that occurs at the cellular level, playing an important role in the growth and maintenance of the body, as well as resistance to environmental changes (Fig. 4A). Food intake and energy expenditure of the body is precisely balanced through the homeostatic pathways located in the hypothalamus of the brain. Metabolic syndrome is a condition in which the body's metabolic homeostasis is disturbed, leading to various complications. Many health organizations around the world are using various biomarkers to diagnose metabolic syndrome. A patient that has three or more of the following five symptoms is diagnosed with a metabolic syndrome: obesity, hypertension, high triglyceride levels, reduced high-density lipoprotein cholesterol, and elevated fasting glucose levels. Of the five symptoms, three criteria including obesity, hypertension, and elevated fasting glucose levels were considered when designing a simplified algorithm for diagnosing metabolic disorders as shown in Fig. 4B as they could be equally applied to either gender. In this algorithm, synaptic devices were used as "AND" and "OR" Boolean logic gates to diagnose metabolic syndrome for patients with two or more of the three symptoms. By using synaptic devices, which are analog-type processors, it is possible to easily implement reconfigurable AND/OR logic gates and switch between the functions of AND and OR as needed. For obese people, having either high blood pressure or elevated fasting glucose levels lead to the diagnosis of metabolic syndrome (OR). On the other hand, for nonobese people, both symptoms needed to be present for the diagnosis of metabolic syndrome (AND). A reconfigurable synaptic logic gate based on the simple combination of one LTS and two STSs was developed to implement the diagnostic algorithm in the reconfigurable synaptic logic (Fig. 4C). The LTS was used to modulate the base current of the entire device via a preset V_{WC} to determine the whether the synaptic logic gate operates as an AND or OR gate. At the same time, the two STSs were used for the logic computation of real-time data. The connected V_{WC} terminals serve as a logic input port for the reconfigurable logic gate. The detailed circuit

diagram and optical microscope image of the logic gate are shown in Fig. 4 (D and E), where a reconfigurable synaptic logic gate consisting of three synaptic transistors is connected in parallel between the pre- and postsynaptic terminals. V_{WC1} refers to the gate terminal connected to the LTS that modulates the overall current of the reconfigurable logic via V_{preset} to switch between the AND and OR operations. Logic operations are performed through V_{WC} pulses applied to the gate terminals (V_{WC2} and V_{WC3}) of the two STSs. V_{WC} pulses of 0 and -2 V were used for binary logic inputs of "0" and "1," respectively. The output current of the reconfigurable synaptic logic gate was compared against a threshold value ($30 \mu\text{A}$) to distinguish whether the logic output is 0 or 1. $|PSC|$ values above and below the threshold value were considered as logic values of 1 and 0, respectively. Figure 4F shows the real-time $|PSC|$ plot of the reconfigurable synaptic logic gate when the weight of the LTS is at its original state. When a logic value of 1 was input to only one of the two STSs, the logic gate outputted a value of 0. On the other hand, when a logic value of 1 was input to both STSs, the $|PSC|$ exceeded the threshold value and outputted a value of 1, indicating that the reconfigurable synaptic logic operates as an AND gate. Next, 20 update pulses were input to the LTS to set the retention current of the reconfigurable synaptic logic to $10 \mu\text{A}$, and the same logic inputs were applied to the STSs (Fig. 4G). For the synaptic logic gate with a preset LTS, a logic value of 1 input to one or more of the STSs resulted in a $|PSC|$ exceeding the threshold value, corresponding to the OR operation. The truth table for the logic input and output values for the reconfigurable synaptic logic gate is shown in Fig. 4H.

To further investigate the feasibility of the reconfigurable synaptic logic for implementing the diagnostic algorithm, we inputted various biomarker data from the human body. First, to convert values of various biomarkers into V_{WC} inputs for logic operations, we precisely examined the peak $|PSC|$ of the STS under varying V_{WC} inputs as shown in Fig. 5A. V_{WC} pulses with amplitudes varying from 0 to -2 V in steps of -0.1 V were applied to STS. Figure 5B plots the peak $|PSC|$ extracted from the real-time graph as a function of the input V_{WC} amplitude. The peak PSC of the STS undergoes a relatively minor change for V_{WC} levels less than -1 V but then increases rapidly for V_{WC} levels above -1 V. In addition, the peak PSC exceeded the predetermined threshold current of $10 \mu\text{A}$ for a V_{WC} of -1.8 V or higher. Next, V_{WC} amplitudes corresponding to biomarker levels were set on the basis of statistical data. Figure 5C shows statistical distributions of fasting blood glucose and blood pressure levels for the Korean population in 2020 divided into three main sections. In the case of fasting blood glucose, people with common values below 100 mg/ml were labeled as "normal" and classified as section 1 (green). People with fasting blood glucose levels between 100 and 109 mg/ml , also called the "cautionary" level, were classified as section 2 (orange). People with fasting blood glucose levels of 110 mg/ml or higher, which is the diagnostic criterion for metabolic syndrome, were classified into section 3 (red). Similarly, concerning systolic blood pressure (SBP), normal ranges below 120 mmHg were defined as section 1, higher ranges from 120 to 129 mmHg were defined as the cautionary level (section 2), and levels above 130 mmHg were defined as the metabolic syndrome diagnostic criteria (sections 3 and higher). On the basis of statistical data, a V_{WC} of -1 V, corresponding logic input of 0, was applied to the STS for the first section (normal level). For sections 3 and above ("metabolic syndrome" level), a V_{WC} of -2

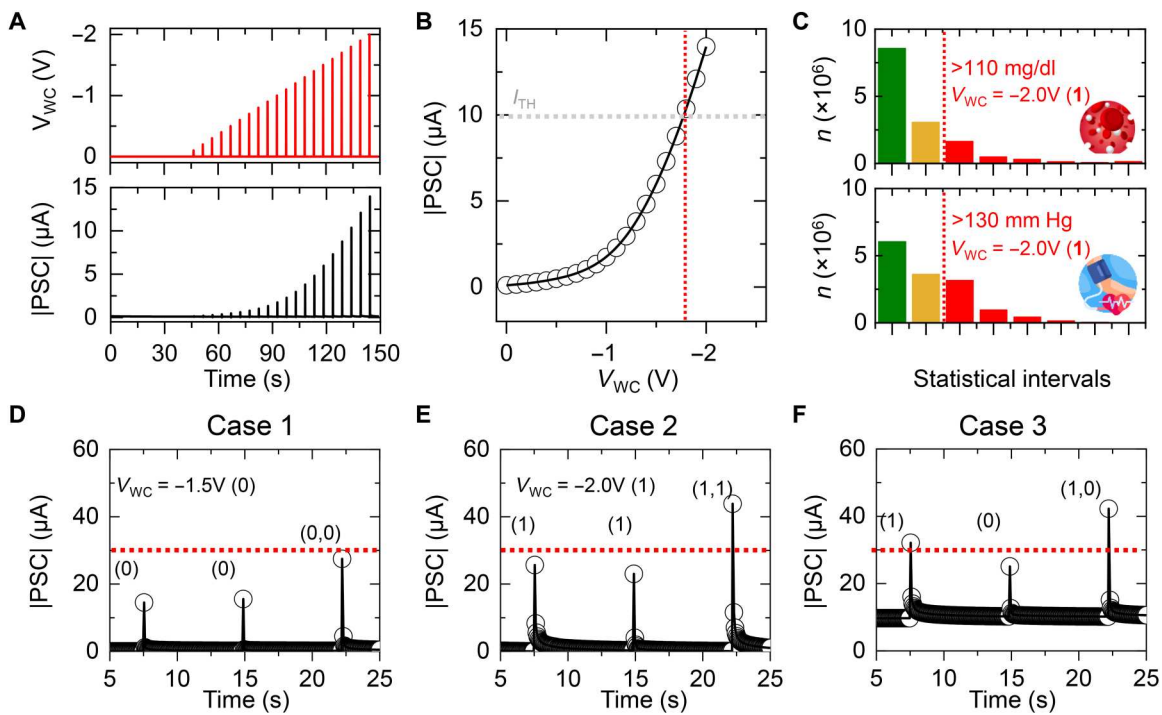


Fig. 5. Confirmation of the reconfigurable synaptic logic with statistical data. (A) Excitatory postsynaptic current (EPSC) response of the short-term synapse (STS) under varied pulse amplitude. (B) A plot of peak |postsynaptic current (PSC)| as a function of the amplitude of V_{WC} . (C) Distribution status of systolic blood pressure (SBP) and fasting blood glucose in the Korean population. The statistical graphs were plotted on the basis of the disclosed data from the National Health Insurance Service of Korea. (D to F) Real-time |PSC| plots of the analog-type operator under varied case inputs: Case 1 simulated a normal person (D), case 2 simulated a person with normal body weight but high SBP and fasting glucose levels (E), and case 3 simulated an overweighted person having one of high SBP or fasting glucose levels (F).

V , corresponding to a logic input of 1, was set as the input of the STS. Furthermore, for section 2 (cautionary level), an input V_{WC} of 1.5 V, which corresponds to a logical value of 0 but with a distinguishable PSC, was applied to the STS. Note that the use of an intermediate V_{WC} that leads to a slightly elevated PSC that is still below the threshold is to use the characteristics of a neuromorphic device based on analog signal processing. The reconfigurable synaptic logic only switches from an AND gate to an OR gate when the LTS is set to have a retention PSC above 10 μ A for the obese case [body mass index (BMI) over 25; fig. S8]. Case 1 simulates a person without metabolic syndrome, but with cautionary SBP and fasting blood glucose levels. Cases 2 and 3 simulate the biometric profile of people with metabolic syndrome. In case 2, the simulated person is not obese but has SBP and fasting blood glucose levels that exceed the threshold and classify as section 3 or above. The simulated person in case 3 is obese but has either high SBP levels or high fasting blood glucose levels, not both. For device operation, V_{WC} values were first sequentially inputted to STS₁ and STS₂ to check the reliability of individual devices, and then the V_{WC} values were simultaneously inputted to perform the logic operation. Figure 5 (D to F) shows the real-time |PSC| plots of the analog-type operator for the input sets of cases 1 to 3. In case 1, V_{WC} inputs of -1.5 V were applied simultaneously, but the PSC current remained under the threshold value indicating the logic output of 0. In case 2, the output PSC exceeded the threshold only when 1 was input to both STSs simultaneously (logic input of "11" for the AND operation). Case 3 exhibited a |PSC| that exceeded the threshold with only one 1 at the logic input due to the previously set LTS current

(corresponding with the OR operation). Overall, the analog-type operator was able to implement the diagnostic algorithm successfully to recognize metabolic syndrome in several simulated biometric profiles with high accuracy.

Last, to further verify the potential of the analog-type operator to be used as a processor for a wearable health care device that needs to process cascading data from multiple sensors with varied update periods, we proposed an appetite control system for metabolic assistance by integrating the operator with wearable sensors. Figure S9 shows the schematic diagram of how the hypothalamus integrates peripheral signals to maintain metabolic homeostasis. The brain's specialized neural network controls the amount of food intake by promoting or suppressing appetite based on metabolic data collected through various peripheral signal pathways. Representative peripheral data typically involved in appetite control include total body fat, blood glucose levels, and gastrointestinal status. Fat cells accumulated in the human body release a hormone called leptin that suppresses appetite. In addition, the residual chemical energy from metabolic processes is stored in fat cells and enhances the release of leptin, resulting in the steady suppression of appetite. On the other hand, the metabolic response to instantaneous events such as food intake is driven by hormones such as insulin and ghrelin. Increased blood glucose levels after a food intake stimulate the secretion of insulin, which promotes the storage of blood glucose in body cells and suppresses appetite. At the same time, an expanded stomach due to food intake inhibits the release of ghrelin, a hormone produced in the stomach that stimulates appetite. Continuously or temporarily secreted from peripheral organs, these

hormones bind to respective receptors in the hypothalamus and generate nerve signals. Furthermore, the generated neural signals are integrated and processed through a neural network to properly control appetite and sustain metabolic homeostasis. Figure 6A presents a schematic diagram of a data processing system integrating an analog-type operator with wearable sensor data to simulate the functions of a biological neural network. Two STSs are used to process nonstatic biomarker signals such as blood glucose levels and stomach status that are periodically updated, whereas a single LTS is used to process BMI data that are rather static. Resistance-based wearable physical and chemical sensors were simulated respectively using electrospun conductive wires and oxide semiconductors (fig. S10). The resistance change of the sensors modulates the amplitude of the V_{WC} inputs to the STSs through the voltage divider circuit (figs. S11 to S13). Twenty consecutive V_{WC} pulses were applied to the STSs to sufficiently update the sensor data. A PSC of the operator that exceeds a set threshold triggers an alert that appetite suppression is required. To minimize energy consumption, the PSC of the device was quickly measured through a V_{READ} of -0.01 V for a short time after the weight update. The detailed operation process of the sensor operator–integrated system is illustrated in Fig. 6B. The base PSC level according to the BMI index was first set by the retention current of the LTS. Then, stomach status and blood glucose data were updated to the STSs, yielding a

combined signal at the output PSC of the analog-type operator. Last, the operation of the wearable appetite control system was simulated, where pre- and postmeal human body data were processed by the operator, and the resulting PSC was compared against a threshold value. Typically, human blood glucose levels are maintained at a baseline level of around 100 mg/dl and gradually increase proceeding carbohydrate absorption after the beginning of a meal, reaching peak levels in about 60 min. After peaking, glucose levels gradually decrease over a period of 2 to 3 hours and return to baseline levels. The postprandial gastrointestinal changes and variations in blood glucose levels were consulted from the medical reports (49–53). On the basis of this data, the typical physiological changes occurring after a meal were hypothesized over time and used as data for the simulation. Gastric distention rate and blood glucose levels were set by assuming fasting, eating, digestion, and postprandial activity conditions in accordance with the postprandial blood glucose change cycle as shown in Fig. 6C. PSCs of the analog-type operator corresponding to simulated data from normal and obese people are shown in Fig. 6(D and E). The threshold level, which is the basis for generating an appetite suppressant alert signal, was set to 10 μ A. The PSC of nonobese individuals increased from 0.19 to 9.52 μ A following meal intake and then gradually returned to initial levels. In the case of obese individuals, the PSC, which was 3.54 μ A before meals, increased to a maximum of 19.49 μ A after meals, under the

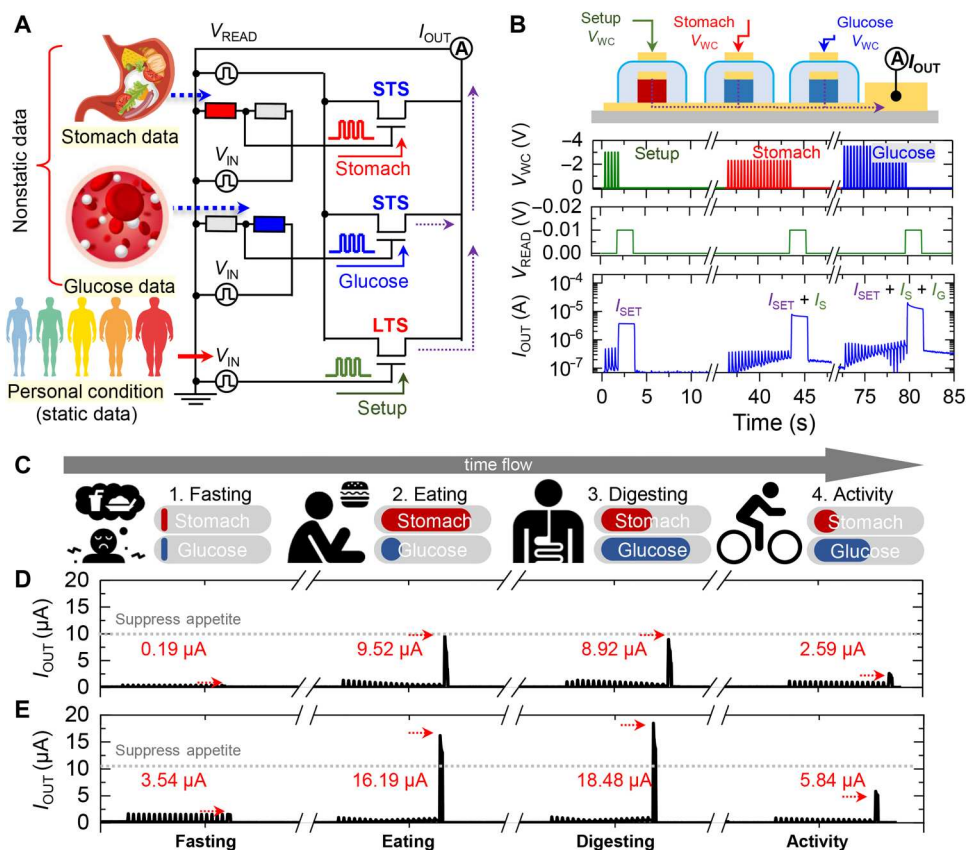


Fig. 6. Evaluation of the sensor operator–integrated system for metabolic monitoring. (A) Schematic illustration of the sensor operator–integrated system. (B) Proof-of-concept illustration and operation plots of the sensor operator–integrated system. (C to E) Schematic illustration of the human stomach and blood glucose level during a meal cycle (C) and the corresponding output currents of the sensor operator device under simulation of a normal person (D) and obese person cases (E). STS, short-term synapse; LTS, long-term synapse.

same V_{WC} inputs. Figure S14 plots the retention current of the LTS and reads PSC of the appetite control system in nonobese and obese cases. In the case of a nonobese person, the PSC remained under the threshold level, whereas an obese person generated a PSC exceeding the threshold level for a long period. This indicates that the wearable analog-type operator presented here has great potential to be used as an appetite control device to help treat metabolic syndrome. Moreover, the efficient computing performance of the synaptic processors has demonstrated considerable potential to be used in the future as a wearable health care device that can handle various time-dependent biomedical information in combination with wearable biosensors.

DISCUSSION

In this study, we demonstrated a technique to selectively define STS and LTS in a crossbar synapse array via a photochemical reaction. The photoreactive cross-linking agent contained in the organic channel successfully controlled ion migration through the electrolyte-gated vertical synapse, enabling the selective fabrication of STSs and LTSs. The STS displayed a large change in synaptic current in response to an input signal but recovered to its original state within a few seconds. On the other hand, the LTS exhibited a long-lasting PSC for more than a few minutes with the same input. In addition, the memory properties of the synapse were modulated by controlling the UV exposure time and the resultant degree of photochemical reaction. Last, selectively defined LTSs and STSs were combined to implement a small-sized hardware neural network to be used for various biomedical applications. The reconfigurable synaptic logic gate, switchable between the AND and OR logic operations, was successfully configured to implement an algorithm for diagnosing metabolic syndrome. Furthermore, the potential for the synaptic processor was demonstrated by verifying the feasibility of an appetite control device for treating metabolic disorders through the integration of wearable sensors and reconfigurable synaptic logic. We expect that implementing the analog-type operator constructed by the selective definition of LTSs and STSs as presented above will not only be used in various biomedical applications but also provide a distinctive approach for developing neuromorphic computing.

MATERIALS AND METHODS

Materials

Processing solvents such as acetone, chloroform, and 2-propanol were purchased from Sigma-Aldrich. P3HT (regioregular, average Mn: 54,000 to 75,000), For photo-patternable ion gel, poly(ethylene glycol)diacrylate monomer and 2-hydroxy-2-methylpropiofophenone were also purchased from Sigma-Aldrich. 1-Ethyl-3-methylimidazolium bis(trifluoromethyl sulfonyl)imide ionic liquid was purchased from TCI Chemicals. The azide cross-linker 2Bx was synthesized and confirmed by the nuclear magnetic resonance spectroscopy as previously reported (42, 46–48). The electrical properties of the vertical synaptic device and logic gates were measured using a Keithley 4200 electrometer.

Device fabrication

P3HT solution dissolved in chloroform at a concentration of 5 mg/ml was blended with 2Bx solution [2Bx (5 mg/ml) in chloroform] in a ratio of 19:1. The blended solution was spin-coated on the bottom

electrode (thermally deposited Cr/Au with 1/17-nm thickness on SiO₂/Si⁺⁺ wafer) at 1500 rpm for 30 s. The sample was dried for 12 hours in an Ar-purged glovebox. After fully drying the sample, the P3HT channels were defined by conventional photolithography, followed by reactive ion etching under O₂ plasma. After removing the residual photoresist by acetone, the cross-linking reaction to define LTS was performed under selective UV irradiation (254 nm and 1000 W/cm²) through a photo mask for varied times from 1 to 7 s. Next, the top and gate electrodes (1/40 nm of Cr/Au) were thermally deposited using a metal shadow mask. Last, ion gel was patterned using a different UV source (365 nm, 100 mW/cm²) as previously reported (54).

Equations for nonlinearity calculation

The NL value of the LTP/D curve was calculated using the following equations:

$$G_{LTP} = B \cdot [1 - \exp(-P/A_p)] + G_{min} \quad (1)$$

$$B = (G_{max} - G_{min})/[1 - \exp(-P_{max}/A_p)] \quad (2)$$

where G_{LTP} is the conductance value of the LTP curve, P is the number of applied pulses, A is a parameter representing NL, and B is a fitting constant used to normalize the conductance range. The A value was extracted from the experimental data using the MATLAB code provided as an open source (55), and the corresponding NL values were derived from tables provided by the same source.

Supplementary Materials

This PDF file includes:

Figs. S1 to S14

REFERENCES AND NOTES

- H. C. Ates, P. Q. Nguyen, L. Gonzalez-Macia, E. Morales-Narváez, F. Güder, J. J. Collins, C. Dincer, End-to-end design of wearable sensors. *Nat. Rev. Mater.* **7**, 887–907 (2022).
- M. Bariya, H. Y. Y. Nyein, A. Javey, Wearable sweat sensors. *Nat. Electron.* **1**, 160–171 (2018).
- K. Bayoumi, M. Gaber, A. Elshafeey, O. Mhameed, E. H. Dineen, F. A. Marvel, S. S. Martin, E. D. Muse, M. P. Turakhia, K. G. Tarakji, M. B. Elshazly, Smart wearable devices in cardiovascular care: Where we are and how to move forward. *Nat. Rev. Cardiol.* **18**, 581–599 (2021).
- R. Ghaffari, D. S. Yang, J. Kim, A. Mansour, J. A. Wright Jr., J. B. Model, D. E. Wright, J. A. Rogers, T. R. Ray, State of sweat: Emerging wearable systems for real-time, noninvasive sweat sensing and analytics. *ACS Sens.* **6**, 2787–2801 (2021).
- J. Kim, A. S. Campbell, B. E.-F. de Ávila, J. Wang, Wearable biosensors for healthcare monitoring. *Nat. Biotechnol.* **37**, 389–406 (2019).
- C. Kittanawong, A. J. Rogers, K. W. Johnson, Z. Wang, M. P. Turakhia, J. L. Halperin, S. M. Narayan, Integration of novel monitoring devices with machine learning technology for scalable cardiovascular management. *Nat. Rev. Cardiol.* **18**, 75–91 (2021).
- G.-H. Lee, H. Moon, H. Kim, G. H. Lee, W. Kwon, S. Yoo, D. Myung, S. H. Yun, Z. Bao, S. K. Hahn, Multifunctional materials for implantable and wearable photonic healthcare devices. *Nat. Rev. Mater.* **5**, 149–165 (2020).
- J. R. Sempionatto, J. A. Lasalde-Ramírez, K. Mahato, J. Wang, W. Gao, Wearable chemical sensors for biomarker discovery in the omics era. *Nat. Rev. Chem.* **6**, 899–915 (2022).
- Z. Abedjan, N. Boujema, S. Campbell, P. Casla, S. Chatterjea, S. Consoli, C. Costa-Soria, P. Czech, M. Despenic, C. Garattini, D. Hamelinck, A. Heinrich, W. Kraaij, J. Kustra, A. Lojo, M. M. Sanchez, M. A. Mayer, M. Melideo, E. Menasalvas, F. M. Aarestrup, E. N. Artigot, M. Petković, D. R. Recupero, A. R. Gonzalez, G. R. Kerremans, R. Roller, M. Romao, S. Ruping, F. Sasaki, W. Spek, N. Stojanovic, J. Thoms, A. Vasiljevs, W. Verachtert, R. Wuyts, Data science in healthcare: Benefits, challenges and opportunities, in *Data Science for Healthcare*:

- Methodologies and Applications*, S. Consoli, D. Reforgiato Recupero, M. Petković, Eds. (Springer International Publishing, 2019), pp. 3–38.
10. C. Krittawong, A. J. Rogers, M. Aydar, E. Choi, K. W. Johnson, Z. Wang, S. M. Narayan, Integrating blockchain technology with artificial intelligence for cardiovascular medicine. *Nat. Rev. Cardiol.* **17**, 1–3 (2020).
 11. K.-H. Yu, A. L. Beam, I. S. Kohane, Artificial intelligence in healthcare. *Nat. Biomed. Eng.* **2**, 71–731 (2018).
 12. W. Gao, S. Emaminejad, H. Y. Nyein, S. Challal, K. Chen, A. Peck, H. M. Fahad, H. Ota, H. Shiraki, D. Kiriyu, D.-H. Lien, G. A. Brooks, R. W. Davis, A. Javey, Fully integrated wearable sensor arrays for multiplexed *in situ* perspiration analysis. *Nature* **529**, 509–514 (2016).
 13. H. Jeong, J. Y. Lee, K. Lee, Y. J. Kang, J.-T. Kim, R. Avila, A. Tzavelis, J. Kim, H. Ryu, S. S. Kwak, J. U. Kim, A. Banks, H. Jang, J.-K. Chang, S. Li, C. K. Mummidisetti, Y. Park, S. Nappi, K. S. Chun, Y. J. Lee, K. Kwon, X. Ni, H. U. Chung, H. Luan, J.-H. Kim, C. Wu, S. Xu, A. Banks, A. Jayaraman, Y. Huang, J. A. Rogers, Differential cardiopulmonary monitoring system for artifact-canceled physiological tracking of athletes, workers, and COVID-19 patients. *Sci. Adv.* **7**, eabg3092 (2021).
 14. S. Kim, B. Lee, J. T. Reeder, S. H. Seo, S.-U. Lee, A. Hourlier-Fargette, J. Shin, Y. Sekine, H. Jeong, Y. S. Oh, A. J. Aranyosi, S. P. Lee, J. B. Model, G. Lee, M.-H. Seo, S. S. Kwak, S. Jo, G. Park, S. Han, I. Park, H.-I. Jung, R. Ghaffari, J. Koo, P. V. Braun, J. A. Rogers, Soft, skin-interfaced microfluidic systems with integrated immunoassays, fluorometric sensors, and impedance measurement capabilities. *Proc. Natl. Acad. Sci.* **117**, 27906–27915 (2020).
 15. Y. Yang, Y. Song, X. Bo, J. Min, O. S. Pak, L. Zhu, M. Wang, J. Tu, A. Kogan, H. Zhang, T. K. Hsiai, Z. Li, W. Gao, A laser-engraved wearable sensor for sensitive detection of uric acid and tyrosine in sweat. *Nat. Biotechnol.* **38**, 217–224 (2020).
 16. C. Zhu, A. Chortos, Y. Wang, R. Pfattner, T. Lei, A. C. Hinckley, I. Pochorovski, X. Yan, J. W. F. To, J. Y. Oh, J. B.-H. Tok, Z. Bao, B. Murmann, Stretchable temperature-sensing circuits with strain suppression based on carbon nanotube transistors. *Nat. Electron.* **1**, 183–190 (2018).
 17. P. Gutruf, V. Krishnamurthi, A. Vázquez-Guardado, Z. Xie, A. Banks, C.-J. Su, Y. Xu, C. R. Haney, E. A. Waters, I. Kandela, S. R. Krishnan, T. Ray, J. P. Leshock, Y. Huang, D. Chanda, J. A. Rogers, Fully implantable optoelectronic systems for battery-free, multimodal operation in neuroscience research. *Nat. Electron.* **1**, 652–660 (2018).
 18. S. M. Won, E. Song, J. T. Reeder, J. A. Rogers, Emerging modalities and implantable technologies for neuromodulation. *Cell* **181**, 115–135 (2020).
 19. S. Niu, N. Matsuhisa, L. Beker, J. Li, S. Wang, J. Wang, Y. Jiang, X. Yan, Y. Yun, W. Burnett, A. S. Y. Poon, J. B.-H. Tok, X. Chen, Z. Bao, A wireless body area sensor network based on stretchable passive tags. *Nat. Electron.* **2**, 361–368 (2019).
 20. S. M. Won, L. Cai, P. Gutruf, J. A. Rogers, Wireless and battery-free technologies for neuroengineering. *Biomed. Eng.* **7**, 405–423 (2023).
 21. E. J. Fuller, S. T. Keene, A. Melianas, Z. Wang, S. Agarwal, Y. Li, Y. Tuchman, C. D. James, M. J. Marinella, J. J. Yang, A. Salleo, A. A. Talin, Parallel programming of an ionic floating-gate memory array for scalable neuromorphic computing. *Science* **364**, 570–574 (2019).
 22. D. Ielmini, H.-S. P. Wong, In-memory computing with resistive switching devices. *Nat. Electron.* **1**, 333–343 (2018).
 23. K. Roy, A. Jaiswal, P. Panda, Towards spike-based machine intelligence with neuromorphic computing. *Nature* **575**, 607–617 (2019).
 24. A. Melianas, T. J. Quill, G. LeCroy, Y. Tuchman, H. V. Loo, S. T. Keene, A. Giovannitti, H. R. Lee, I. P. Maria, I. McCulloch, A. Salleo, Temperature-resilient solid-state organic artificial synapses for neuromorphic computing. *Sci. Adv.* **6**, eabb2958 (2020).
 25. Y. van de Burgt, E. Lubberman, E. J. Fuller, S. T. Keene, G. C. Faria, S. Agarwal, M. J. Marinella, A. Alec Talin, A. Salleo, A non-volatile organic electrochemical device as a low-voltage artificial synapse for neuromorphic computing. *Nat. Mater.* **16**, 414–418 (2017).
 26. Y. van de Burgt, A. Melianas, S. T. Keene, G. Malliaras, A. Salleo, Organic electronics for neuromorphic computing. *Nat. Electron.* **1**, 386–397 (2018).
 27. Q. Xia, J. J. Yang, Memristive crossbar arrays for brain-inspired computing. *Nat. Mater.* **18**, 309–323 (2019).
 28. X. Xu, Y. Ding, S. X. Hu, M. Niemier, J. Cong, Y. Hu, Y. Shi, Scaling for edge inference of deep neural networks. *Nat. Electron.* **1**, 216–222 (2018).
 29. Y. Choi, S. Oh, C. Qian, J.-H. Park, J. H. Cho, Vertical organic synapse expandable to 3D crossbar array. *Nat. Commun.* **11**, 4595 (2020).
 30. S. Ham, M. Kang, S. Jang, J. Jang, S. Choi, T.-W. Kim, G. Wang, One-dimensional organic artificial multi-synapses enabling electronic textile neural network for wearable neuromorphic applications. *Sci. Adv.* **6**, eaba1178 (2020).
 31. H. Han, H. Yu, H. Wei, J. Gong, W. Xu, Recent progress in three-terminal artificial synapses: From device to system. *Small* **15**, 1900695 (2019).
 32. S. Kim, S. Kim, D. H. Ho, D. G. Roe, Y. J. Choi, M. J. Kim, U. J. Kim, M. L. Le, J. Kim, S. H. Kim, J. H. Cho, Neurorobotic approaches to emulate human motor control with the integration of artificial synapse. *Sci. Adv.* **8**, eabo3326 (2022).
 33. S. Kim, D. G. Roe, Y. Y. Choi, H. Woo, J. Park, J. I. Lee, Y. Choi, S. B. Jo, M. S. Kang, Y. J. Song, S. Jeong, J. H. Cho, Artificial stimulus-response system capable of conscious response. *Sci. Adv.* **7**, eabe3996 (2021).
 34. Y. Kim, A. Chortos, W. Xu, Y. Liu, J. Y. Oh, D. Son, J. Kang, A. M. Foudeh, C. Zhu, Y. Lee, S. Niu, J. Liu, R. Pfattner, Z. Bao, T.-W. Lee, A bioinspired flexible organic artificial afferent nerve. *Science* **360**, 998–1003 (2018).
 35. Y. Lee, J. Y. Oh, W. Xu, O. Kim, T. R. Kim, J. Kang, Y. Kim, D. Son, J. B.-H. Tok, M. J. Park, Z. Bao, T.-W. Lee, Stretchable organic optoelectronic sensorimotor synapse. *Sci. Adv.* **4**, eaat7387 (2018).
 36. Y. H. Liu, L. Q. Zhu, P. Feng, Y. Shi, Q. Wan, Freestanding artificial synapses based on laterally proton-coupled transistors on chitosan membranes. *Adv. Mater.* **27**, 5599–5604 (2015).
 37. S. Seo, S.-H. Jo, S. Kim, J. Shim, S. Oh, J.-H. Kim, K. Heo, J.-W. Choi, C. Choi, S. Oh, D. Kuzum, H. S. P. Wong, J.-H. Park, Artificial optic-neural synapse for colored and color-mixed pattern recognition. *Nat. Commun.* **9**, 5106 (2018).
 38. K. M. Song, J.-S. Jeong, B. Pan, X. Zhang, J. Xia, S. Cha, T.-E. Park, K. Kim, S. Finizio, J. Raabe, J. Chang, Y. Zhou, W. Zhao, W. Kang, H. Ju, S. Woo, Skyrmion-based artificial synapses for neuromorphic computing. *Nat. Electron.* **3**, 148–155 (2020).
 39. Z. Wang, S. Joshi, S. Savel'ev, W. Song, R. Midya, Y. Li, M. Rao, P. Yan, S. Asapu, Y. Zhuo, H. Jiang, P. Lin, C. Li, J. H. Yoon, N. K. Upadhyay, J. Zhang, M. Hu, J. P. Strachan, M. Barnell, Q. Wu, H. Wu, R. S. Williams, Q. Xia, J. J. Yang, Fully memristive neural networks for pattern classification with unsupervised learning. *Nat. Electron.* **1**, 137–145 (2018).
 40. L. F. Abbott, W. G. Regehr, Synaptic computation. *Nature* **431**, 796–803 (2004).
 41. J. Moon, W. Ma, J. H. Shin, F. Cai, C. Du, S. H. Lee, W. D. Lu, Temporal data classification and forecasting using a memristor-based reservoir computing system. *Nat. Electron.* **2**, 480–487 (2019).
 42. M. J. Kim, M. Lee, H. Min, S. Kim, J. Yang, H. Kweon, W. Lee, D. H. Kim, J.-H. Choi, D. Y. Ryu, M. S. Kang, B. Kim, J. H. Cho, Universal three-dimensional crosslinker for all-photopatterned electronics. *Nat. Commun.* **11**, 1520 (2020).
 43. T. Ohno, T. Hasegawa, T. Tsuruoka, K. Terabe, J. K. Gimzewski, M. Aono, Short-term plasticity and long-term potentiation mimicked in single inorganic synapses. *Nat. Mater.* **10**, 591–595 (2011).
 44. A. Giovannitti, D.-T. Sbircea, S. Inal, C. B. Nielsen, E. Bandiello, D. A. Hanifi, M. Sessolo, G. G. Malliaras, I. McCulloch, J. Rivnay, Controlling the mode of operation of organic transistors through side-chain engineering. *Proc. Natl. Acad. Sci.* **113**, 12017–12022 (2016).
 45. K. H. Seol, S. J. Lee, K. G. Cho, K. Hong, K. H. Lee, Highly conductive, binary ionic liquid-solvent mixture ion gels for effective switching of electrolyte-gated transistors. *J. Mater. Chem. C* **6**, 10987–10993 (2018).
 46. R.-Q. Png, P.-J. Chia, J.-C. Tang, B. Liu, S. Sivaramakrishnan, M. Zhou, S.-H. Khong, H. S. O. Chan, J. H. Burroughes, L.-L. Chua, R. H. Friend, P. K. H. Ho, High-performance polymer semiconducting heterostructure devices by nitrene-mediated photocrosslinking of alkyl side chains. *Nat. Mater.* **9**, 152–158 (2010).
 47. S. Wang, J. Xu, W. Wang, G.-J. N. Wang, R. Rastak, F. Molina-Lopez, J. W. Chung, S. Niu, V. R. Feig, J. Lopez, T. Lei, S.-K. Kwon, Y. Kim, A. M. Foudeh, A. Ehrlich, A. Gasperini, Y. Yun, B. Murmann, J. B. H. Tok, Z. Bao, Skin electronics from scalable fabrication of an intrinsically stretchable transistor array. *Nature* **555**, 83–88 (2018).
 48. J. Yang, D. Hahn, K. Kim, S. Rhee, M. Lee, S. Kim, J. H. Chang, H. W. Park, J. Lim, M. Lee, H. Kim, J. Bang, H. Ahn, J. H. Cho, J. Kwak, B. Kim, C. Lee, W. K. Bae, M. S. Kang, High-resolution patterning of colloidal quantum dots via non-destructive, light-driven ligand crosslinking. *Nat. Commun.* **11**, 2874 (2020).
 49. D. E. Cummings, J. Q. Purnell, R. S. Frayo, K. Schmidova, B. E. Wisse, D. S. Weigle, A pre-prandial rise in plasma ghrelin levels suggests a role in meal initiation in humans. *Diabetes* **50**, 1714–1719 (2001).
 50. S. Daenen, A. Sola-Gazagnes, J. M'Bemba, C. Dorange-Breillard, F. Defer, F. Elgrably, É. Larger, G. Slama, Peak-time determination of post-meal glucose excursions in insulin-treated diabetic patients. *Diabetes Metab.* **36**, 165–169 (2010).
 51. K. Esposito, M. Cirotta, D. Carleo, B. Schisano, L. Sardelli, D. Di Tommaso, L. Misso, F. Saccocciano, A. Ceriello, D. Giugliano, Post-meal glucose peaks at home associate with carotid intima-media thickness in type 2 diabetes. *J. Clin. Endocrinol. Metab.* **93**, 1345–1350 (2008).
 52. F. Kong, R. P. Singh, Disintegration of solid foods in human stomach. *J. Food Sci.* **73**, R67–R80 (2008).
 53. T. Shiya, M. Nakazato, M. Mizuta, Y. Date, M. S. Mondal, M. Tanaka, S.-I. Nozoe, H. Hosoda, K. Kangawa, S. Matsukura, Plasma ghrelin levels in lean and obese humans and the effect of glucose on ghrelin secretion. *J. Clin. Endocrinol. Metab.* **87**, 240–244 (2002).
 54. Y. Choi, J. Kang, D. Jariwala, M. S. Kang, T. J. Marks, M. C. Hersam, J. H. Cho, Low-voltage complementary electronics from ion-gel-gated vertical van der waals heterostructures. *Adv. Mater.* **28**, 3742–3748 (2016).
 55. P. Y. Chen, X. Peng, S. Yu, in *2017 IEEE International Electron Devices Meeting (IEDM)* (IEEE, 2017), pp. 6.1.1–6.1.4.

Acknowledgments

Funding: This research was supported by the National Research Foundation (NRF) of Korea grant funded by the Korea government (MSIT) (RS-2023-00234581) and BrainLink program funded by the Ministry of Science and ICT through the NRF of Korea (RS-2023-00237308). This project was partially supported by Sloan Research Fellowship and Heritage Medical Research Institute. **Author contributions:** Y.C. conducted the fabrication, analysis, and measurement of the synaptic devices and analog-type operator. D.H.H., S.K., Y.J.C., and D.G.R. gave general advice on measuring and analysis of synaptic properties. I.C.K. assisted preparing and processing of 28x photocrosslinker. J.M. and H.H. assisted in the study design, device test, and writing the manuscript. W.G. guided the overall direction for biomedical applications of

neuromorphic devices. J.H.C. initiated the research and designed the overall experiments. All authors discussed the results and contributed to the paper. **Competing interests:** The authors declare that they have no competing interests. **Data and materials availability:** All data needed to evaluate the conclusions in the paper are present in the paper and/or the Supplementary Materials.

Submitted 8 January 2023
Accepted 30 May 2023
Published 5 July 2023
10.1126/sciadv.adg5946

Science Advances

Physically defined long-term and short-term synapses for the development of reconfigurable analog-type operators capable of performing health care tasks

Yongsuk Choi, Dong Hae Ho, Seongchan Kim, Young Jin Choi, Dong Gue Roe, In Cheol Kwak, Jihong Min, Hong Han, Wei Gao, and Jeong Ho Cho

Sci. Adv., **9** (27), eadg5946.
DOI: 10.1126/sciadv.adg5946

View the article online

<https://www.science.org/doi/10.1126/sciadv.adg5946>

Permissions

<https://www.science.org/help/reprints-and-permissions>

Downloaded from https://www.science.org on July 06, 2023

Use of this article is subject to the [Terms of service](#)

Science Advances (ISSN) is published by the American Association for the Advancement of Science. 1200 New York Avenue NW, Washington, DC 20005. The title *Science Advances* is a registered trademark of AAAS.

Copyright © 2023 The Authors, some rights reserved; exclusive licensee American Association for the Advancement of Science. No claim to original U.S. Government Works. Distributed under a Creative Commons Attribution NonCommercial License 4.0 (CC BY-NC).